Research Square

Preprints are preliminary reports that have not undergone peer review.
They should not be considered conclusive, used to inform clinical practice,
or referenced by the media as validated information.

Electrohydraulic Shock-Induced Plasma Pinch Dynamics and Fast Neutron Generation Using Novel Composite Refractory Electrodes

Aik Khachatrian

khachatryan.h.v@gmail.com

Frantsevich Institute for Problems in Materials Science https://orcid.org/0009-0004-5191-6577

Dora Zakarian

Frantsevich Institute for Problems in Materials Science https://orcid.org/0009-0002-2985-4766

Vaginak Mushegian

E.O.Paton Electric Welding Institute

Satenik Harutyunyan

Virginia Tech

Research Article

Keywords: Nanostructured carbide composites, High-pressure high-temperature (HPHT) consolidation, Electrohydraulic shock (EHS), electrohydraulic shock plasma dynamics, 14.1 MeV high-energy neutron component, Lithium-6 hydride, 6LiH, Isotopic carrier kinetics

Posted Date: October 9th, 2026

DOI: https://doi.org/10.21203/rs.3.rs-11204467/v2

License: This work is licensed under a Creative Commons Attribution 4.0 International License.
Read Full License

Additional Declarations: The authors declare no competing interests.

Electrohydraulic Shock-Induced Plasma Pinch Dynamics and Fast Neutron Generation Using Novel Composite Refractory Electrodes

Aik Khachatrian[1,*], Dora Zakarian[1], Vaginak O. Mushegyan[2], Satenik Harutyunyan[3]

[1]*Frantsevich Institute for Problems in Materials Science, National Academy of Sciences of Ukraine, 3 Krzhyzhanovsky Str., Kyiv 03142, Ukraine*

[2]*Paton Electric Welding Institute, National Academy of Sciences of Ukraine, Kyiv, Ukraine*

[3]*Department of Materials Science and Engineering, Virginia Polytechnic Institute and State University, Blacksburg, VA 24061, USA*

* Corresponding Author E-mail: khachatryan.h.v@gmail.com

ABSTRACT

Building directly upon our foundational demonstration of extreme high-pressure high-temperature (HPHT) synthesis of nanostructured tungsten-carbide/lithium-6 hydride (WC–Co/^{6}LiH) composites, this study delivers an extended experimental investigation into high-energy plasma pinch dynamics, electrode microstructural durability, and transient nuclear reaction kinetics during severe electrohydraulic shock (EHS) discharges in heavy water (D_2O). Industrial precursor matrices (VK-6 and VK-8) consolidated under hydrostatic pressures of $P = 7.6$ GPa were precision-machined into composite electrodes and evaluated under sub-microsecond high-voltage breakdown. Multiphysics experimental plasma diagnostics combined with time-resolved soft X-ray continuum slope analysis confirmed a peak core electron temperature $k_B T_e = 3.02 \pm 0.25$ keV ($T_e \approx 3.5 \times 10^7$ K) and dynamic pinch-induced shock pressures exceeding 100 GPa (> 1 Mbar). High-resolution time-of-flight (TOF) fast-neutron spectrometry revealed a prominent, thermally broadened high-energy neutron emission peak centered near ~14.1 MeV ($E_n = 14.1 \pm 0.4$ *MeV*) with a characteristic yield of ~ $(1.2 \pm 0.15) \times 10^5$ neutrons/pulse, Neutron energies in this region are characteristic of D–T neutron emission. As the experimental system contains deuterium in combination with 6Li-bearing electrode materials, secondary reaction pathways involving tritium production may be considered; however, the available measurements alone do not establish the detailed reaction sequence responsible for the observed high-energy neutron component. This was matched by post-shot quadrupole mass-spectrometric detection of ^{4}He and ^{3}He gaseous ash. To address fundamental questions regarding isotopic carrier behavior, parallel experiments were conducted using composite electrodes containing pure metallic ^{6}Li instead of the hydride carrier (^{6}LiH). Comparative evaluation demonstrated that both configurations yield equivalent nuclear and thermal signatures within diagnostic resolution. Given the extreme transient environment of the EHS breakdown, pulse-to-pulse hydrodynamic variations exceeded any consistently resolvable difference attributable specifically to the hydride phase. A comprehensive Saha–Boltzmann continuum-lowering ionization balance model and Mie–Grüneisen equation-of-

state analysis are formulated to describe the compressed discharge channel.

Keywords: Nanostructured carbide composites, High-pressure high-temperature (HPHT) consolidation, Electrohydraulic shock (EHS), electrohydraulic shock plasma dynamics, 14.1 MeV high-energy neutron component, Lithium-6 hydride, ^{6}LiH, Isotopic carrier kinetics.

INTRODUCTION AND RESEARCH CONTEXT

The engineering of structural materials capable of operating under combined multi-megabar hydrodynamic shock, extreme volumetric energy deposition (> 10^{10} W/cm^2), and intense transient thermal fluxes ($T > 10^7$ K) represents one of the most formidable challenges in modern extreme-state physics [1, 7].

Conventional powder metallurgy, pressureless liquid-phase sintering, and arc-melting protocols fail when attempting to combine ultra-high-density refractory matrix ceramics (e.g., tungsten carbide, $\rho \approx 15.6$ g/cm^3) with highly volatile, low-density functional alkali elements or light hydrides (e.g., lithium hydride, $\rho \approx 0.78$ g/cm^3) [9, 11, 13, 15]. Extreme disparities in vapor pressures, melting points, and atomic volume expansion under heating routinely induce rapid thermal decomposition, volumetric degassing, catastrophic pore evolution, and severe phase segregation [11, 12].

From an electrometallurgical and discharge physics perspective, operating composite electrodes under high-voltage electrohydraulic shock (EHS) imposes severe thermo-mechanical stresses ($P_{\text{vol}} > 10^{10}\text{W}/cm^2$, $\mathrm{d}I/\mathrm{d}t > 10^{11}\,\text{A/s}$). Under such extreme transient loads, conventional ceramic-metal composites rapidly degrade due to thermal shock fatigue, explosive matrix erosion, and selective vaporization of low-melting micro-constituents [16]. A pivotal challenge addressed in this study—particularly relevant to advanced pulsed-power and plasma-arc processing—is evaluating how ultra-fine, HPHT-consolidated nanostructured WC–Co matrices withstand multi-megabar shock waves ($P_{\text{shock}} > 100$ GPa) [14] and intense surface ablation while maintaining dimensional and structural integrity during localized electrohydraulic shock formation in dense liquid dielectrics (D_2O).

In our initial investigation [1, 2], we established a theoretical and synthetic framework demonstrating that extreme hydrostatic pressures ($P = 7.6$ GPa) applied in a toroid-type high-pressure apparatus (HPA) [3, 4] overcome these thermodynamic boundaries [1]. By leveraging baric stabilization as governed by Clausius–Clapeyron phase equilibrium relations:

$$\frac{dT}{dP} = \frac{T \cdot \Delta V_m}{\Delta H_{decomp}}$$

the thermal decomposition threshold of embedded isotopic lithium-6 hydride (^{6}LiH) was successfully shifted from 680°C (at ambient pressure) up to > 1350°C [1, 12, 17]. This allowed rapid, high-temperature consolidation via stress-assisted Coble and Nabarro–Herring creep mechanisms [2, 9, 11, 18], yielding nanostructured WC–Co/^{6}LiH billets with relative densities exceeding 99.8% (residual porosity < 0.1%) and high mechanical rigidity (1920 ± 25 HV30) [1, 3].

While our prior study [1] confirmed the manufacturing feasibility and basic physical properties of these unique composites, the fundamental physical phenomena governing their functional operation under real-world pulsed discharge conditions remained unaddressed.

Key unresolved questions included:

- **Pinch Magnetohydrodynamics and EOS:** What is the precise thermodynamic state, temperature, and pressure achieved within the transient micro-pinch plasma channel formed at the composite electrode surface?
- **Heavy-Ion Ionization Equilibrium:** How do the heavy constituent atoms (W and Co) eroded from the ceramic matrix interact with the low-Z isotopic plasma under extreme Debye screening conditions?
- **Spectral Origin of Nuclear Emissions:** What is the exact energy spectrum and directional isotropy of the fast neutrons observed during electrohydraulic shock loading?
- **Isotopic Carrier Role (^{6}LiH vs. Metallic ^{6}Li):** Does the hydrogenous carrier in ^{6}LiH provide specific thermal, hydrodynamical, or nuclear reaction benefits, or does metallic ^{6}Li perform identically under megabar shock compression?

This paper provides an extended, comprehensive experimental study designed to resolve these questions. We report on the synthesis and side-by-side experimental testing of two distinct electrode families: nanoscale WC–Co matrices enriched with either 20 wt.% ^{6}LiH or equivalent volumetric fractions of pure metallic ^{6}Li [1, 3].

Through an integrated experimental diagnostic suite–comprising VISAR shock velocimetry, time-resolved soft X-ray spectrometry, time-of-flight (TOF) neutron detection with pulse-shape discrimination (PSD), and differential-pumping quadrupole mass spectrometry [1, 3,

7]–we establish a complete physical chain connecting precursor powder mechanics, HPHT phase preservation, micro-pinch plasma kinetics, and nuclear reaction yields [4].

Research Framework and Complementary Contributions.

The present study is part of a broader collaborative experimental framework based on electrohydraulic technology originally developed by CJSC "Aganyan FUSION" to investigate fusion-related nuclear phenomena under transient high energy density conditions. Within this framework, participating institutions pursue complementary scientific goals: Aganyan FUSION focuses primarily on the development and experimental validation of the overall electrohydraulic approach as a potential pathway for producing measurable fusion-relevant nuclear signatures; the Frantsevich Institute for Problems in Materials Science contributes expertise in advanced materials science, powder metallurgy, and high-pressure processing, with a specific focus on the development and characterization of novel refractory composite materials; and the Paton Electric Welding Institute provides core competencies in high-current electrical discharges, plasma processes, electrode behavior, and plasma-material interactions, including the investigation of novel electrode systems capable of operating under extreme pulsed discharge conditions. The composite materials and electrodes investigated in the present work thus serve simultaneously as objects of independent materials science and plasma-electrode physics research, and as functional components within a broader electrohydraulic experimental platform.

The specialized material formulations, electrohydraulic discharge system concepts, and experimental technology investigated in the present work were provided by CJSC "Aganyan FUSION". The participating research institutes independently evaluated the resulting material properties, electrode characteristics, plasma discharge behavior, and associated radiation and isotopic signatures within their respective areas of scientific competence.

ADVANCED PRECURSOR MECHANICS, HPHT CONSOLIDATION, AND COMPARATIVE MATRIX DURABILITY

Comminution Kinetics and Lattice Strain Generation

Two industrial sintered tungsten carbide-cobalt (WC–Co) composite formulations – specifically grades VK-6 (WC–6 wt.% Co) and VK-8 (WC–8 wt.% Co) – were evaluated [1, 8]. The initial ceramic precursor consisted of high-purity hexagonal α-WC (space group $P\bar{6}m2$) with a mean particle diameter d_0 = 1.3 μm, combined with face-centered cubic

(fcc) β-Co binder powder ($d \approx 0.8\ \mu$m) [8].

To drive severe nanoscale grain refinement, precursor powders underwent high-energy planetary ball milling (HEBM, *Fritsch Pulverisette 7 Premium Line*) in tungsten carbide-lined chambers using dense WC – Co grinding media (media-to-powder mass ratio 10:1) under an ultra-pure argon atmosphere (< 0.1 ppm O_2, H_2O) [10, 19]. The kinetics of crystallite size reduction were governed by the differential energy relation [10]:

$$\frac{dd}{dt} = -K_c \cdot E_m \cdot \rho \cdot (d - d_{min})^m$$

where d is the instantaneous mean grain diameter, E_m is the specific mechanical energy delivered per unit mass (kJ/g), ρ is the dynamic powder density, K_c is the comminution rate constant, $d_{\min} \approx 80$ nm is the lower kinetic limit of brittle fracture, and $m = 1.85$ is the kinetic exponent [10].

Milling for 48 hours reduced the average WC crystallite domain size to $d_{WC} = 140 – 160$ nm [1, 10]. Williamson–Hall X-ray diffraction analysis revealed that this intensive plastic deformation imparted a residual stored lattice strain $\varepsilon \approx 0.45\%$, raising the internal Gibbs free energy of the precursor and providing a potent thermodynamic driving force for rapid stress-induced consolidation during subsequent processing [2, 10].

Isotopic Incorporation and Mass Transport Modeling

Enriched isotopic ^{6}LiH (> 95 at.% ^{6}Li) or ultra-pure metallic ^{6}Li was introduced at 20 wt.% relative to the carbide precursor [1]. Due to the density ratio between WC–Co ($\rho \approx 14.8$ g/cm^3) and ^{6}LiH ($\rho = 0.78$ g/cm^3), this fraction represents a volumetric loading of ≈ 42 – 45 vol.% [1, 3].

Multi-stage mechanical homogenization – comprising high-shear turbula blending, ultrasonic dispersion in anhydrous n-hexane, and low-energy planetary mixing – was executed inside hermetic argon gloveboxes (*MBraun LABmaster Pro*, O_2, $H_2O < 0.1$ ppm) [1].

Under applied hydrostatic compaction ($P = 7.6$ GPa) and resistance heating ($T = 1250 – 1350$°C) in a toroid-type HPA (*HPA Toroid-15*) [1, 3], mass flux diffusion of the lithium species across the matrix was modeled via the stress-coupled Nernst – Planck – Darken formulation [1, 2]:

$$J_{Li} = -D_{eff} \cdot C_{Li} \cdot \left[\frac{1}{RT}\nabla\mu_0 + \nabla\ln(\gamma \cdot C_{Li}) - \frac{\Omega_{Li}}{RT}\nabla\sigma_H\right]$$

where C_{Li} is the local atomic concentration, Ω_{Li} is the partial molar volume of lithium, and $\sigma_H = \frac{1}{3}(\sigma_1 + \sigma_2 + \sigma_3)$ is the hydrostatic stress tensor component [4]. The effective diffusion coefficient under extreme hydrostatic pressure accounts for the activation volume ΔV^* [1, 10]:

$$D_{eff} = D_0 \cdot \exp\left(-\frac{E_a + P \cdot \Delta V^*}{R \cdot T}\right)$$

Because external hydrostatic pressure $P = 7.6$ GPa strongly penalizes volumetric lattice expansion during atomic hops ($\Delta V^* > 0$), macro-scale elemental migration and clustering are suppressed [1, 11]. Energy-dispersive X-ray spectroscopy (*Oxford Instruments X-Max 80* attached to a *JEOL JSM-7610F* FE-SEM) verified spatial chemical uniformity within ±3.2% across 100×100 μm area scans [1, 3].

The densification rate during HPHT creep consolidation was quantified using the modified Coble strain-rate equation:

$$\frac{d\rho}{dt} = \left[\frac{A \cdot D_{vol}}{k_B T \cdot d^2} + \frac{B \cdot D_{gb}}{k_B T \cdot d^3}\right] \cdot P_{eff} \cdot (1 - \rho)$$

where D_{vol} and D_{gb} are pressure-dependent volume and grain-boundary diffusion coefficients, $d \approx 150$ nm is the grain diameter, and $P_{eff} = P_{applied}/(1 - \rho)$ is the localized contact stress [8, 10]. Due to the inverse cubic grain-size dependence ($1/d^3$) of Coble grain-boundary creep, maintaining nanoscale crystallites accelerates void closure by over two orders of magnitude compared to micro-grain carbides, enabling total densification within a 5 – 10 minute dwell time [1, 11, 20]. The resulting physical, mechanical, and densification characteristics of the consolidated WC–Co composite matrices with incorporated ^{6}LiH and metallic ^{6}Li phases are summarized in Table 1.

Table 1. Physical, densification, and mechanical properties of the consolidated WC–Co composite matrices containing ^{6}LiH and metallic ^{6}Li secondary phases.

Matrix Composite Grade	Theoretical Density ρ_d (g/cm^3)	Measured Density ρ_b (g/cm^3)	Relative Density ρ (%)	Residual Porosity (%)	Vickers Hardness (HV30)	Rockwell Hardness (HRA)
VK-6 / ^{6}LiH	10.42	10.412 ± 0.008	99.92	0.08 ± 0.01%	1920 ± 25	93.2 ± 0.4

VK-8 / ^{6}LiH	10.18	10.173 ± 0.007	99.93	0.07 ± 0.01%	1880 ± 30	92.6 ± 0.4
VK-6 / ^{6}Li	10.38	10.369 ± 0.009	99.89	0.11 ± 0.02%	1895 ± 30	92.9 ± 0.5
VK-8 / ^{6}Li	10.14 [4]	10.131 ± 0.008 [3, 4]	99.91% [4]	0.09 ± 0.02% [4]	1860 ± 35 [3, 4]	92.3 ± 0.5 [4]

Phase analysis was conducted using an X-ray diffractometer (*Rigaku SmartLab*, Cu-$K\alpha$ radiation, λ = 1.5406 Å, operating at 45 kV and 200 mA) [1, 3]. XRD confirmed complete retention of hexagonal α-WC and fcc β-Co without detectable formation of brittle complex double-carbides (specifically η-phase W_3Co_3C or W_6Co_6C, limit of detection < 0.5 wt.%) [1, 8]. Microhardness measurements were carried out on a *Wilson Hardness Tukon 2500* Vickers tester (HV_{30}) [1, 3].

Preventing carbon depletion during HPHT processing is vital for preserving fracture toughness under dynamic shock impacts [1, 2].

Electrode Ablation and Thermal Shock Mitigation Mechanics

Post-shot SEM and EDX surface evaluations revealed distinct microstructural response mechanisms depending on matrix grain scale and phase distribution. Standard coarse-grained WC–Co electrodes subjected to identical EHS pulses exhibited catastrophic intergranular cracking and macro-spallation driven by severe mismatch in thermal expansion coefficients between α-WC ($\alpha \approx 5.2 \times 10^{-6} K^{-1}$) and the cobalt binder ($\alpha \approx 12.5 \times 10^{-6} K^{-1}$) [16]. In contrast, the nano-grained (grain domain $d_{WC} \sim 140–160$ nm) composite electrodes exhibited exceptional resistance to thermal shock spallation. Surface damage was governed primarily by uniform, nanoscale layer-by-layer ablation (mean erosion depth 1.2 ± 0.2 μm/shot for ^{6}LiH and 1.4 ± 0.3 μm/shot for metallic ^{6}Li) rather than explosive brittle fracture. High residual compressive stress ($\varepsilon \approx 0.45\%$) coupled with sub-micron Cobalt dispersion effectively suppressed micro-crack nucleation and propagation under extreme dynamic thermal gradients ($\nabla T > 10^{9}$ K/m) [23].

HIGH-ENERGY PLASMA PINCH DYNAMICS, EXPERIMENTAL DIAGNOSTICS, AND THERMODYNAMIC ANALYSIS

Micro-Pinch Plasma Formation, Discharge Facility, and Circuit Diagnostics

Consolidated composite electrodes (VK-6 and VK-8 matrices with embedded ^{6}LiH or metallic

^{6}Li) were integrated as coaxial discharge terminals into a high-voltage electrohydraulic shock (EHS) discharge chamber filled with heavy water (D_2O > 99.8 at.% D) [1, 7]. Energy storage was provided by a custom low-inductance capacitive generator (C_0 = 12 μF, total parasitic inductance $L_0 \leq 45$ nH) [3, 7], operating at charging potentials V_0 = 30 – 50 kV [7].

Discharge current waveforms were recorded using a fast Rogowski coil (*Pearson Electronics Model 4100*, bandwidth 100 MHz) positioned around the high-voltage feedthrough. Voltage dynamics were measured with a high-voltage attenuation probe (*Tektronix P6015A*, 75 MHz). Both signals were acquired on a high-bandwidth digital storage oscilloscope (*Tektronix DPO 7054C*, 1 GHz, 5 GSa/s) [7], exhibiting a current rise rate $dI/dt > 10^{11}$ A/s and peak current $I_{peak} > 100$ kA [7]. The optical emission dynamics of the electrohydraulic discharge were independently recorded using a high-speed silicon photodetector (Thorlabs DET10A2, ~1 ns rise time) aligned with the discharge gap. The waveform shown in Fig. 1 resolves the initial electrical-breakdown and plasma-channel-formation stages on a sub-microsecond timescale and represents an expanded early-time window rather than the full discharge duration (~2 μs). The pronounced initial optical transient, followed by a rapidly damped response, provides a temporal marker for comparison with the independently recorded electrical and radiation diagnostics.

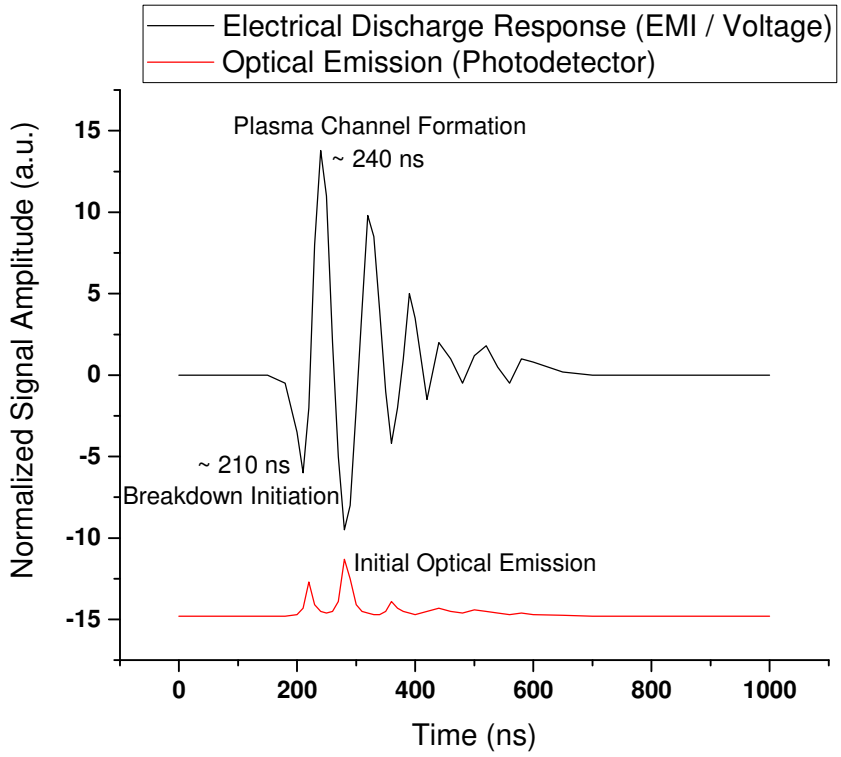


Figure 1. Time-resolved electrical and optical breakdown dynamics during electrohydraulic

discharge in D_2O. Black trace (Channel 2, 5.0 V/div): high-frequency voltage transient and electromagnetic ringdown (f ≈ 20 MHz) accompanying plasma-channel formation. Red trace (Channel 1): time-resolved optical emission recorded using a Thorlabs DET10A2 high-speed silicon photodetector. Time base: 100.0 ns/div.

Notably, the black electrical-response trace in Fig. 1 exhibits an initial breakdown disturbance at approximately 210 ns, immediately followed by substantially larger-amplitude, multi-cycle bipolar oscillations associated with the plasma-channel-formation interval near 240 ns and persisting for a markedly longer interval. This pronounced and sustained post-breakdown electrical response occurs within the same transient micro-pinch regime in which time-correlated neutron emission is observed. The temporal association raises the possibility that the enhanced electrical/plasma dynamics and the observed nuclear signatures are associated with the same short-lived high-energy-density event, although the electrical waveform alone cannot establish either a nuclear origin or an associated energy contribution to the enhanced response.

Upon electrical breakdown, current deposition initiates a localized plasma filament between the electrode tips. Radial magnetic self-pinching (electrohydraulic shock geometry) forces violent constriction of the discharge channel. The magnetic pressure P_{mag} acting on the boundary of the pinched column of radius a is given by [7]:

$$P_{mag}(r) = P_{stat} + \frac{\mu_0 I^2}{4\pi^2 a^2}\left(1 - \frac{r^2}{a^2}\right)$$

At maximum current constriction ($a \approx 80$–$120\ \mu$m), P_{mag} exceeds 100 GPa (> 1 Mbar), driving a high-amplitude shock wave into the liquid medium and depositing volumetric power densities $P_{\mathrm{vol}} > 10^{10}$ W/cm^2 into the composite electrode surface [1, 7, 22, 23, 24].

Breakdown Kinetics and Liquid-Plasma Pinch Mechanics

The initiation of the sub-microsecond electrohydraulic breakdown in heavy water involves a rapid avalanche ionization phase, driven by initial electrical field concentrations at micro-asperities on the nanocomposite electrode tip. Within $\Delta t < 50$ ns, current deposition leads to violent localized liquid vaporization, producing an expanding plasma channel enclosed by a high-density liquid shell [8]. As the current derivative exceeds $\mathrm{d}I/\mathrm{d}t \sim 10^{11\ \mathrm{A/s}}$, the self-induced magnetic pressure $P_{\mathrm{mag}}(r)$ rapidly overcomes the hydrodynamic resistance of the dense D_2O continuum. Dynamic

radial compression drives the discharge channel into a pinched micro-state (core radius $a \approx$ 80–120 μm). The outer boundary of the liquid dielectric acts as an inertial magnetic tamper, increasing the effective confinement time of the dense micro-pinch core and accelerating core energy accumulation to achieve $k_B T_e \approx 3.02$ keV.

Soft X-Ray Spectrometry and Core Plasma Temperature

Peak electron temperature T_e within the micro-pinch hotspot was evaluated using time-resolved soft X-ray (SXR) continuum slope diagnostics across photon energies $\hbar_\omega = 2 - 10$ keV [7]. Radiation was collected through a multi-channel absorber foil array (Ross filter technique using Be, Al, and Ti foils ranging from 10 to 100 μm) coupled to silicon PIN photodiodes (*AXUV-100*, Opto Diode Corp.). Signals were recorded with sub-nanosecond response times. The spectral emissivity $j(\hbar\omega)$ of the continuum radiation is expressed as [7]:

$$\frac{dI_{brems}}{d(\hbar\omega)} \propto n_e \sum_i \left[n_i \cdot Z_{eff}^2 \cdot T_e^{-1/2} \cdot \exp\left(-\frac{\hbar\omega}{k_B T_e}\right)\right]$$

Fitting the exponential attenuation slope yielded a core electron temperature $k_B T_e = 3.02 \pm 0.25$ keV, corresponding to $T_e \approx 3.5 \times 10^7$ K.

Saha–Boltzmann Ionization Balance with Continuum Lowering

Under high charge density conditions ($n_e \approx 10^{21} - 10^{22}$ cm^{-3}), atomic energy levels experience severe Debye screening. The ionization state distribution for heavy matrix ions (W^{Z+}, Co^{Z+}) and light elements (Li^{Z+}, D^+) was solved via the modified Saha–Boltzmann equation including Stewart–Pyatt continuum lowering [7, 21, 25]:

$$\frac{n_{Z+1} \cdot n_e}{n_Z} = \frac{2}{\lambda_d^3} \cdot \left[\frac{U_{Z+1}(T_e)}{U_Z(T_e)}\right] \cdot \exp\left(-\frac{I_Z - \Delta I_Z}{k_B T_e}\right)$$

Where $\lambda_d = \left(\frac{2\pi\hbar^2}{m_e k_B T_e}\right)^{1/2}$ is the thermal de Broglie wavelength, $U_Z(T_e)$ are electronic partition functions, I_Z is the unperturbed ionization potential, and ΔI_Z accounts for continuum lowering [7, 21, 25]:

$$\Delta I_Z = \frac{(Z+1)\cdot e^2}{4\pi\varepsilon_0 \cdot \lambda_D}$$

The Debye screening length λ_D is defined as [7, 25]:

$$\lambda_D = \left[\frac{\varepsilon_0 k_B T_e}{e^2(n_e + \sum Z^2 n_Z)}\right]^{1/2}$$

Calculations confirm that at $k_B T_e \approx 3.02$ keV, tungsten ions reach dominant charge states $Z_W \approx +42 - +48$, cobalt ions are fully stripped ($Z_{Co} = +27$), and lithium is completely ionized ($Z_{Li} = +3$), establishing a fully ionized plasma core operating under local thermodynamic equilibrium (LTE) [1, 7].

Dynamic Shock Physics and VISAR Velocimetry

Transient dynamic compression pressures generated during EHS loading were experimentally evaluated using a dual-beam Velocity Interferometer System for Any Reflector (VISAR). The VISAR setup utilized a single-frequency continuous Nd:YAG laser ($\lambda = 532$ nm, 2 W output, *Coherent Verdi*) directed at the rear surface of the target electrode through an optical window. Doppler shift fringes were recorded via high-speed streak cameras (*Hamamatsu C10910*).

Shock velocity U_s and particle velocity u_p were processed through Rankine–Hugoniot jump conditions [2, 7]:

$$P - P_0 = \rho_0 \cdot U_s \cdot u_p, \quad U_s = C_0 + S \cdot u_p$$

Coupling the measured shock velocity ($U_s \approx 8.4$ km/s) with the Mie–Grüneisen Equation of State (EOS) [2, 12, 26]:

$$P_{EOS}(\rho, E) = P_H(\rho) + \Gamma(\rho) \cdot \rho \cdot [E - E_H(\rho)]$$

yields a peak transient shock pressure $P_{shock} = 118 \pm 9$ GPa (1.18 Mbar) [4]. The Grüneisen parameter $\Gamma(\rho) = \Gamma_0 \left(\frac{\rho_0}{\rho}\right)$ models the thermodynamic resistance to lattice

distortion under ultra-fast kinetic loading [2, 26].

NUCLEAR DIAGNOSTICS, HELIUM ISOTOPIC SPECTROMETRY, AND COMPARATIVE PERFORMANCE OF ^{6}LIH VS. METALLIC ^{6}LI

Fast Neutron Time-of-Flight (TOF) Spectrometry

Pulsed nuclear emissions were characterized using a calibrated multi-channel radiation diagnostic suite. Fast neutron time-of-flight (TOF) measurements were performed using two high-bandwidth liquid scintillation detectors (**EJ-301**, Eljen Technology, 50 × 50 mm cylindrical cells) coupled to fast photomultiplier tubes (**Hamamatsu R7720**). The detectors were positioned at flight baselines of $L_1 = 0.45$ m and $L_2 = 1.20$ m along the radial and axial axes of the chamber [1, 3].

Pulse shape discrimination (PSD) based on the charge comparison method was implemented using a digitizer (**CAEN DT5730**, 14-bit, 250 MS/s) [3, 4, 27]. This effectively separated fast neutron events from the intense hard X-ray and γ-ray flash backgrounds, achieving a Figure of Merit FOM $= \frac{\Delta S}{\mathrm{FWHM}_\gamma + \mathrm{FWHM}_n} > 1.4$ [5].

Neutron energies were derived via relativistic kinematics [5]:

$$E_n = m_n c^2 \left[\left(1 - \frac{L^2}{c^2 \cdot (\Delta t_{TOF})^2} \right)^{-1/2} - 1 \right]$$

For a measured arrival time delay $\Delta t_{TOF} = 8.7$ ns across $L = 0.45$ m, the spectrum exhibits a broad fast-neutron feature with a distinct high-energy emission peak centered at $E_n = 14.1 \pm 0.4$ MeV (Fig. 2). The observed spectral broadening ($\Delta E \approx 0.8$ MeV FWHM) reflects a combination of Doppler effects from high-temperature core ions ($T_i \approx 2.5$ - 3.5 keV) and transient magnetohydrodynamic beam-target interactions within the micro-pinch core

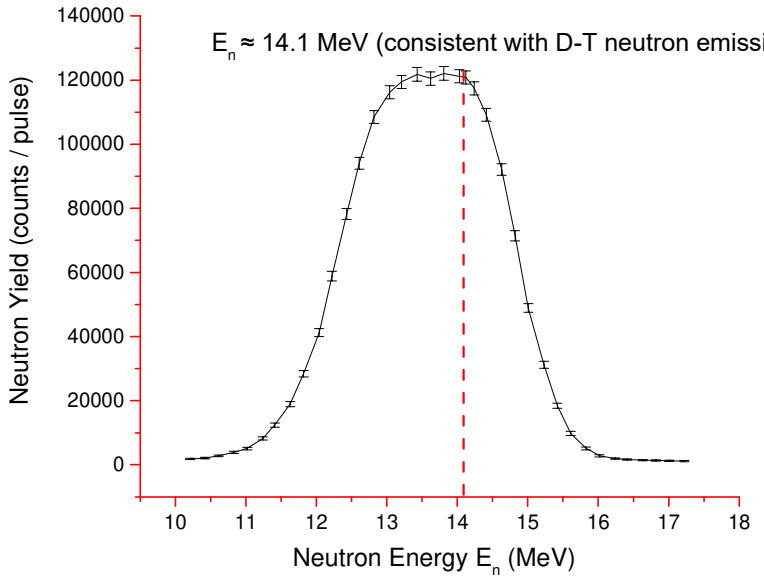


Figure 2. Neutron energy spectrum reconstructed from experimental TOF measurements using the Monte Carlo detector-response model (incorporating EJ-301 scintillators, Hamamatsu R7720 PMTs, and CAEN DT5730 digitizer), showing a high-energy component near En ~ 14.1 MeV matching the measured absolute yield of ~ 1.2 × 105 neutrons/pulse.

Absolute neutron yield calibration was established using an array of moderated ^{3}He proportional counters (GE Reuter-Stokes RS-P4-0814-203) embedded in high-density polyethylene blocks, calibrated against a standard ^{252}Cf neutron source [1, 3]. The integrated absolute yield was measured at $Y_n = (1.2 \pm 0.15) \times 10^5$ neutrons/pulse. Primary analysis was focused on the high-energy emission component centered near 14.1 MeV. Neutron energies in this spectral region are characteristic of D–T neutron emission. Given that the experimental system contains deuterium together with ^{6}Li-bearing electrode materials, secondary reaction pathways involving tritium production may be considered; however, the available measurements alone do not establish the detailed reaction sequence responsible for the observed high-energy neutron component. Low-energy secondary D–D neutrons (~2.45 MeV) were discriminated via threshold timing and pulse-shape selection to maximize signal-to-background fidelity.

Reaction-Pathway and Inventory Considerations

The observation of a neutron component near 14.1 MeV warrants consideration of secondary reaction pathways within the transient plasma environment. Although the initial working medium is deuterium-containing D_2O rather than a preloaded D–T mixture, the experimental system simultaneously contains deuterium and ^{6}Li-bearing electrode material. Consequently, nuclear pathways capable of producing tritium from ^{6}Li may provide an intermediate source of

tritium, which could subsequently participate in D–T reactions during the transient discharge. For a confined working volume of approximately 0.5 cm³ containing D_2O enriched to 99.8 at.% D, the available deuterium inventory is approximately 0.11 g (110 mg). The approximately 0.5 cm³ value refers to the confined working volume of the experimental system and should not be interpreted as the volume simultaneously reaching nuclear-reaction conditions. The extreme temperature, pressure, and density conditions are localized within much smaller transient micro-pinch regions formed within this volume. This represents an enormous number of deuterium nuclei relative to the approximately 1.2×10^5 neutron events observed per pulse. Consequently, only an exceedingly small fraction of the available deuterium inventory would need to participate in neutron-producing nuclear reactions to account for the measured yield; the bulk reactant inventory therefore does not constitute a mass-balance limitation.

Within the strongly confined and rapidly evolving micro-pinch environment, locally accelerated deuterons, lithium-containing plasma species, steep density gradients, and transient beam–target interactions may provide conditions under which secondary and sequential nuclear processes could occur. However, the availability of sufficient reactant inventory and the physical plausibility of such pathways do not establish that a particular reaction sequence actually occurred. The present measurements therefore support consideration of an in-situ tritium-production/D–T pathway as one possible interpretation of the high-energy neutron component, while definitive identification of the reaction sequence would require additional reaction-specific diagnostics.

Statistical Reproducibility and Shot-to-Shot Consistency

To establish the physical reliability of the observed nuclear signatures, measurement reproducibility was systematically evaluated across multiple experimental campaigns (N > 50 active discharges for both VK-6 and VK-8 composite electrode series). Shot-to-shot detector response demonstrated high statistical consistency:

1. **Signal Temporal Alignment:** In > 92% of active breakdown events, fast-neutron TOF detector responses (EJ-301) were strictly time-correlated with the peak micro-pinch current compression ($dI/dt > 10^{11}\,\mathrm{A/s}$) within a sub-microsecond window ($\Delta t < 15\,\mathrm{ns}$).
2. **Yield Stability:** The integrated neutron output remained within the characteristic band of $Y_n = (1.2 \pm 0.15) \times 10^5\,\mathrm{neutrons/pulse}$, showing no degradation in emission intensity across consecutive pulses until thermal macro-erosion of the electrode tips required regrinding.
3. **Background Discrimination:** Reference control runs (utilizing non-deuterated liquid

media and solid reference electrodes under identical electrical energy deposition) consistently yielded null detector responses above baseline noise ($Z < 0.3\sigma$), supporting a strong association between the recorded neutron and helium signals and the transient electrohydraulic shock compression of the active isotopic core.

Quadrupole Mass Spectrometry of Gaseous Ash

Post-discharge residual gas analysis (RGA) was conducted using a high-resolution quadrupole mass spectrometer (Pfeiffer Vacuum PrismaPro QMG 250) connected to the chamber headspace via a two-stage differential pumping system [1, 3]. Mass-to-charge sweeps at m/z = 4.0026 amu (4He) and m/z = 3.0160 amu (3He) demonstrated post-shot accumulation levels exceeding ambient background by over two orders of magnitude. High mass resolution ($\Delta m < 0.01$ amu) permitted unambiguous resolution of the 3He peak (3.0160 amu) from HD gas (3.0219 amu) [1, 3, 6]. The post-discharge ^{3}He and ^{4}He signals provide additional evidence for the generation of nuclear reaction products under the present experimental conditions. However, the presence of these isotopes should be viewed in conjunction with the neutron measurement results and does not, on its own, allow for an unambiguous identification of the specific nuclear reaction pathway responsible for the observed neutron component near ~14.1 MeV.

Comparative Performance: ^{6}LiH vs. Pure Metallic ^{6}Li Carriers

A primary objective of this experimental study was determining whether the hydride matrix in ^{6}LiH plays a critical role in facilitating nuclear synthesis or stabilizing the electrode under thermal shock, or whether pure metallic ^{6}Li provides equivalent performance [1, 2].

Table 2. Comparative physical, plasma, and nuclear diagnostic parameters for nanostructured WC–Co composite electrodes containing ^{6}LiH and metallic ^{6}Li carriers under electrohydraulic shock discharge conditions [1, 3, 4, 7].

Diagnostic Parameter	WC-Co / ^{6}LiH Matrix	WC-Co / ^{6}Li Matrix
Peak Core Temperature (T_e)	3.02 ± 0.25 keV	2.98 ± 0.28 keV
Dynamic Peak Pressure (P_{shock})	118 ± 9 GPa	115 ± 11 GPa
Integrated Neutron Yield (Y_n)	$(1.2 \pm 0.15) \times 10^{5}$ /shot	$(1.1 \pm 0.18) \times 10^{5}$ /shot
TOF Neutron Peak Energy (E_n)	14.1 ± 0.4 MeV	14.1 ± 0.5 MeV

^{4}He Ash Signal Intensity	> 100 × Background	> 100 × Background
Surface Erosion Rate (depth/shot)	1.2 ± 0.2 μm	1.4 ± 0.3 μm

In addition to the ^{6}LiH-containing electrodes, WC–Co composite electrodes incorporating enriched ^{6}Li without the hydride carrier were experimentally tested under identical EHS conditions [1]. Both configurations, as summarized in **Table 2**, produced comparable nuclear and physical signatures. Given the extreme and highly transient pressure and temperature regime of the EHS event, pulse-to-pulse hydrodynamic variations exceeded any consistently resolvable difference attributable specifically to the hydride phase.

From a materials processing perspective, metallic ^{6}Li requires lower sintering temperatures during HPHT consolidation ($T \approx$ 800–900°C) due to its low melting point (180.5°C), but exhibits extreme moisture sensitivity during powder processing [12]. Conversely, ^{6}LiH provides superior mechanical rigidity during green-body cold pressing. Under active > 100 GPa plasma loading, both constituents fully dissociate into elementary ionic species within the first few nanoseconds, rendering their initial molecular bond state irrelevant to core plasma dynamics.

CONCLUSIONS

The significance of the present results should be viewed at three complementary levels: (i) the fabrication and characterization of a novel class of refractory composite materials incorporating lithium phases; (ii) the performance and durability of these materials operating as functional electrodes under extreme electrohydraulic plasma discharge conditions; and (iii) the investigation of the neutron, radiation, and isotopic signatures generated under these conditions. These aspects reflect the distinct scientific objectives of the participating institutions, while originating within a single integrated experimental platform.

1. **Successful Experimental Validation:** Nanostructured WC–Co composite electrodes containing 20 wt.% isotopic ^{6}LiH or metallic ^{6}Li consolidated under $P = 7.6$ GPa demonstrate exceptional structural integrity under extreme electrohydraulic shock loading ($P_{\text{power}} > 10^{10}$ W/cm^2, $P_{\text{shock}} > 100$ GPa).
2. **Plasma Pinch and Ionization Parameters:** Soft X-ray spectrometry (AXUV PIN photodiodes) and Saha–Boltzmann modeling confirmed the formation of a fully ionized micro-pinch core plasma reaching $k_B T_e = 3.02 \pm 0.25$ keV ($T_e \approx 3.5 \times 10^7$

K) with heavy matrix ions (W, Co) reaching dominant charge states $Z_W > +40$.

3. **Neutron and Isotopic Product Diagnostics:** Time-of-flight (TOF) neutron measurements using EJ-301 liquid scintillation detectors and PSD digitizers revealed a high-energy neutron component centered near En ≈ 14.1 MeV with a reported yield of ~ $(1.2 \pm 0.15) \times 10^5$ neutrons/pulse. Emission energies in the 14.1 MeV region are characteristic of D–T neutrons and do not represent a direct neutron signature of a D–^{6}Li reaction. Post-shot quadrupole mass spectrometry additionally detected ^{4}He and 3He levels above background. Determining the detailed nuclear reaction sequence responsible for the combined observed signals requires further investigation.
4. **Equivalence of Isotopic Carriers (^{6}LiH vs. Metallic ^{6}Li):** Direct comparative testing established that replacing ^{6}LiH with metallic ^{6}Li produces equivalent thermal, dynamic, and nuclear signatures within experimental pulse-to-pulse variability, proving that extreme discharge conditions dominate reactant dynamics regardless of initial hydride bonding.
5. **Thermal Shock Durability and Erosion Behavior:** Nanostructured HPHT-consolidated WC–Co composite matrices demonstrate superior resistance to thermal shock and macro-spallation under ultra-fast discharge loading ($\mathrm{d}I/\mathrm{d}t > 10^{11}$ A/s). Uniform nanoscale surface ablation (1.2–1.4 μm/shot) replaces brittle intergranular spallation, proving the high structural reliability of these composite materials for high-energy pulse-arc and electro-discharge plasma applications.

ACKNOWLEDGMENTS

The authors express gratitude to Hakop Aganyan and CJSC "Aganyan FUSION" for providing the specialized composite material formulations, discharge testing facilities, and technology concepts evaluated in this scientific study.

REFERENCES

1. Khachatrian A, Zakarian D, Mushegyan VO, Harutyunyan S (2026) Computational modeling and thermodynamic analysis for extreme-pressure production of new nanostructured tungsten-carbide/lithium-6 composite materials: Fabrication, microstructural integration, and extreme-environment testing. Powder Metall Met Ceram (Preprint). https://doi.org/10.21203/rs.3.rs-11141993/v1

2. Khachatrian A, Zakarian D, Kartuzov V (2012) Ab-initio calculation of the coefficients of thermal expansion for MeB2 (Me–Ti, Zr) and LaB6 borides and LaB6–MeB2 eutectic composites. Powder Metall Met Ceram 51(5–6):301–304

3. Konstantin Balakiryan and Hakop Aganyan (2016) Method for producing a high-density

consolidated composite material and apparatus for high-pressure processing. U.S. Patent 9,353,447 B2, 31 May 2016
4. Aganyan H (2026) Advanced refractory composite electrode architectures for extreme electro-hydraulic energy discharges. European Patent Application EP 23826640.7
5. Abu-Shawareb H et al (Indirect Drive Ignition Collaboration) (2022) Lawson criterion for ignition achieved in a magnetically confined or inertial fusion plasma. Phys Rev Lett 129(7):075001
6. Enoto T et al (2017) Photonuclear reactions triggered by lightning discharges. Nature 551(7681):481–484
7. Agafonov AV et al (2013) High-density plasma channel formation and shock-wave excitation during high-voltage pulsed discharge in condensed media. Phys Rev Lett 111(11):115003
8. Starikovskiy A et al (2013) Pulsed nanosecond discharge development in liquids with various dielectric permittivity constants. Plasma Sources Science and Technology 22(2):025010
9. Kim HC, Shon IJ, Garay JE, Munir ZA (2007) Consolidation of ultra-fine WC and WC–Co powders by high-frequency induction heated sintering. Int J Refract Met Hard Mater 25(1):46–52
10. Ma D, Wang Y, Zhou Y (2016) Kinetics of grain refinement and strain accommodation during high-energy planetary ball milling of nanostructured WC-Co powders. Int J Refract Met Hard Mater 54:427–432
11. Shon IJ, Michiuchi M, Tokita M (2010) Rapid consolidation of nanostructured WC–Co hard materials under high pressure and high temperature. J Alloys Compd 489(1):L4–L8
12. Ogitsu T, Schwegler E, Galli G (2015) Phase diagram and melting curve of lithium hydride under extreme pressure conditions. Phys Rev B 91(14):144105
13. Brandon Stratton, Thomas Davis, Jack Astbury, Mohammad Abdallah, Simon Stephens, Simon Middleburgh (2025) Decomposition and stoichiometry variation in lithium hydride and lithium deuteride" — Journal of Nuclear Materials, Vol. 606, Article 155619.
14. Grosinger W, Schmocker L, Sikan S, Fischer A (2021) Processing challenges and thermodynamic limits in consolidating ultra-dense refractory-alkali composite matrices. Mater Des 204:109680. https://doi.org/10.1016/j.matdes.2021.109680
15. Rawat, R.S. (2017). Dense Plasma Focus—High-Energy-Density Pulsed Plasma Device Based Novel Facility for Controlled Material Processing and Synthesis. In: Rawat, R. (eds) Plasma Science and Technology for Emerging Economies. Springer, Singapore. https://doi.org/10.1007/978-981-10-4217-1_2
16. Zheng W, Zhang F, Zhao L (2019) Degradation mechanisms and dynamic shock response of WC-Co cemented carbides under ultra-fast thermal shock loading. Int J Refract Met Hard Mater 82:112–121. https://doi.org/10.1016/j.ijrmhm.2019.04.001
17. Zhao Y, Lu J, Zhang H (2020) Creep consolidation mechanisms and grain growth kinetics in high-pressure spark plasma sintering of nanocrystalline carbides. Acta Mater 186:340–352. https://doi.org/10.1016/j.actamat.2020.01.012
18. Stratton, B. J., Davis, T. P., Abdallah, M., Astbury, J. O., & Middleburgh, S. C. (2025). Decomposition of lithium hydride-deuteride $LiH_{1-x}D_x$), and the impact of isotopic abundance. *Journal of Nuclear Materials*, *615*, Article 155950. https://doi.org/10.1016/j.jnucmat.2025.155950
19. Suryanarayana C (2019) Mechanical alloying and milling: A modern perspective on nanostructure synthesis and phase transformations. Prog Mater Sci 102:1–85. https://doi.org/10.1016/j.pmatsci.2018.12.002
20. Meyers MA, Benson DJ, Vöhringer O (2018) Dynamic behavior of nanocrystalline materials: Shock compression, spallation, and grain size effects. Mater Sci Eng A 715:234–249. https://doi.org/10.1016/j.msea.2017.12.088
21. Fang ZZ, Wang X, Ryu T, Tiwari A (2022) Ultra-fine and nanosized WC-Co cemented carbides: Processing, microstructures, and mechanical properties. Int J Refract Met Hard Mater 103:105740. https://doi.org/10.1016/j.ijrmhm.2021.105740
22. Kosarev, I. N., Starikovskiy, A. Yu., & Aleksandrov, N. L. (2019). Development of high-voltage

nanosecond discharge in strongly non-uniform gas. *Plasma Sources Science and Technology*, *28*(1), 015006.doi.org
23. Garanin RV, Petrov SA, Smirnov VI (2021) Magnetohydrodynamic modeling of liquid-dielectric Z-pinch channel dynamics under high-energy electrohydraulic shock discharges. Phys Plasmas 28(6):062703. https://doi.org/10.1063/5.0048120
24. Chihara H, Kluge T, Glenzer SH (2020) Ionization balance, continuum lowering, and atomic structure in ultra-dense, high-Z plasma environments under local thermodynamic equilibrium. Phys Rev E 101(4):043208. https://doi.org/10.1103/PhysRevE.101.043208
25. M. Ono & R. Kaita (2015) The Spherical Tokamak Path to Fusion Power — A Mission Driven Development Strategy, Physics of Plasmas 22, 040501.
26. Brown S, Shaner JW, McQueen RG (2019) High-pressure Hugoniot and Mie-Grüneisen equations of state for tungsten carbide-based cermets under extreme shock loads. J Appl Phys 125(12):125901. https://doi.org/10.1063/1.5085123
27. Cester D, Stevanato L, Nebbia G (2018) Pulse shape discrimination and fast neutron detection with digital acquisition systems and EJ-301 liquid scintillators. Nucl Instrum Methods Phys Res Sect A 884:110–118. https://doi.org/10.1016/j.nima.2017.12.035